Supplementary Information, Methods, Tables, and Figures

Finely tuned conformational dynamics regulate the protective function of the MALAT1 triple helix

Abeer A. Ageeli, Kayleigh R. McGovern-Gooch, Magdalena M. Kalinowska, and Nathan J. Baird*
Department of Chemistry & Biochemistry, University of the Sciences, Philadelphia, PA 19143, USA

*To whom correspondence should be addressed:
Tel: 215-596-7396
Fax: 215-596-8543
Email: n.baird@usciences.edu

Supplementary Information

pH dependence of C^+•G-C base triple

UV melting studies by Brown et al. in cacodylate buffer demonstrated that the MALAT1 triplex is stabilized in pH 5 relative to pH 7, consistent with protonation of the cytosine involved in a C^+•G-C base triple[1]. Our studies have been performed in HEPES buffer, pH 7.4 (23 °C). Because the pK_a of HEPES decreases at higher temperature (-0.14 ΔpK_a/10 °C; $pK_{a,20°C}$ = 7.55; $pK_{a,50\ °C}$ = 7.13; $pK_{a,65°C}$ = 6.92), the protonation state of the cytosine involved in the C^+•G-C base triple would be more favorable in a HEPES buffer than in cacodylate buffer (**Supplementary Figure 1**). Therefore, the melting analyses in our study slightly overestimate the thermal stability and are useful for comparative analysis across the range of experimental conditions within our study.

Confirming formation of a triplex in the bi-molecular and tri-molecular constructs

The unimolecular and bimolecular constructs employed in our study are based on several previous studies, including crystal structures of homologous RNA triplexes. A crystal structure of the bimolecular ENE-tail triplex from the KSHV PAN RNA was solved in 2010[2]. A crystal structure of a unimolecular truncated MALAT1 triplex was solved in 2014[3]. A study in 2016 utilized $M1^{ET}$ (our nomenclature) to investigate the role of altered base triple interactions *in vitro* and compared the results with identical mutations made to the full-length RNA *in vivo*[4]. In addition, Brown et al. demonstrated that $M1^{ET}$ competes with $M1^{TH}$ for binding partner METLL16[5]. Hence, the previously published structural and biochemical studies have demonstrated triplex formation for the wild-type, truncated, and bimolecular constructs. It has been suggested that dynamic regulation of this triplex is important *in vivo*, but no studies to date have explored the dynamic properties of this RNA.

Our tri-molecular construct, $M1^{ABsT}$, is derived from the $M1^{ET}$ construct. Furthermore, this construct is similar in design to the decades-old design of DNA triplex forming oligonucleotides (TFO), wherein polypurine/polypyrimidine tracts are identified for targeting with a sequence-specific TFO. In such cases, the sequence of the TFO is designed de novo based on a specific code[6]. Subsequently, complex formation observed by gel shift or spectroscopic melt assays were used to indicate triplex formation. Correlatively, in our study $M1^{A}$ is a purine-rich oligo designed to target the $M1^{BsT}$ duplex in a sequence specific maner in agreement with the triplex design code. We demonstrate complex formation by observation of a single band using electrophoretic mobility shift assay, a single well-defined peak on a size-exclusion column chromatogram, and a cooperative unfolding event during thermal melting.

Finally, the $M1^{AB}$ is a novel construct introduced in our study. We designed this construct consistent with the TFO code and base pairing rules. Because $M1^{B}$ alone can potentially fold into alternative secondary structures, we have carefully determined an annealing protocol to maximize complex formation between $M1^{A}$ and $M1^{B}$. A single band on a gel shift assay and a well-defined peak on size-exclusion column chromatogram again demonstrate a one-to-one association. This construct migrates through the size-exclusion column similarly to the $M1^{ET}$ construct.

Monitoring M1TH thermal melting in HEPES buffer

All thermal melt experiments reported in the main text were performed in HEPES buffer, which has a temperature dependent pKa (ΔpKa = -0.014/°C). At higher temperatures the pH is lowered slightly, affecting the protonation state of the central C^+•G-C triple in the triplex. Therefore, the $T_{m,1}$ are slightly overestimated. **Supplementary Figure 1** demonstrates a maximum ~4.3 °C increase in $T_{m,1}$ over a broad range of ionic conditions relative to the same experiments performed in cacodylate, which has a temperature insensitive pKa. **Supplementary Tables 1 & 2** present $T_{m,1}$ and $T_{m,2}$ values in both HEPES and cacodylate at various pH. The data are consistent with minor differences in T_m in HEPES. Nonetheless, comparisons of the thermal melt data (UV, DS-FRET, DSF) are consistent within each ionic landscape and the interpretations are unaffected by the slight overestimation.

Supplementary Methods

Electrophoretic mobility shift assay

Gel shift analysis using bimolecular and trimolecular constructs were performed using 1 μg of the shortest RNA oligo and addition of 0.5 or 1 molar equivalents of the larger RNA oligo(s). RNA bands were separated on native polyacrylamide electrophoresis in 16.5 mM Tris, 33mM HEPES, and 50 μM EDTA buffer supplemented with 1 mM $MgCl_2$. Gel running buffers were recovered, mixed, and redistributed to the cathode and anode chambers every 30 minutes. Gels were stained with ethidium bromide or SYBR Gold (ThermoFisher).

UV thermal melts in sodium cacodylate buffer

RNAs were annealed and then purified using an Superdex SEC 75 (GE Healthcare) size exclusion chromatography column equilibrated in 20 mM sodium cacodylate, pH 6.7 or pH 7.4, with 1 mM MgCl2. Using this SEC purified RNA, a 500-700 μl sample was prepared in a final RNA concentration of 5 - 10 μg ml^{-1}, 50 mM total monovalent salt (equimolar NaCl and KCl), and the desired magnesium concentration (0.1 and 1 mM). All UV melt experiments were performed in a stoppered 1-cm quartz cuvette. Absorbance was monitored at 260 nm using an Evolusion 300 UV-Vis spectrophotometer (Thermo Scientific) over a temperature range from 20 °C to 85 °C with a 1 °C/min ramp rate. Raw melting profiles and derivatives were plotted using Origin2015 software (OriginLab). The derivative curves were smoothed using Fast Fourier Transform (FTT) 50-point smoothing. The $T_{m,1}$ and $T_{m,2}$ were determined from the smoothed derivative plot using a peak finding algorithm within the software.

[$MgCl_2$] (mM)	$T_{m,1}$ (°C)		$\Delta T_{m,1}$ (°C)	$T_{m,2}$ (°C)		$\Delta T_{m,2}$ (°C)
	HNK pH 7.4	CNK pH 7.4	HNK-CNK	HNK pH 7.4	CNK pH 7.4	HNK-CNK
0.1	53.3 ± 0.7	51.3 ± 0.1	2.0	70.0 ± 0.1	69.5 ± 0.1	0.6
1.0	65.7 ± 1.1	60.8 ± 0.5	4.9	77.7 ± 0.8	76.0 ± 0.2	1.7

Supplementary Table S1. Comparison of T_m for M1TH in HEPES vs. cacodylate buffers using DSF.
Thermal melt experiments at two different concentrations of $MgCl_2$ were performed in the presence of 50 mM monovalent salt (equimolar NaCl and KCl) in 20 mM HEPES or 20 mM sodium cacodylate. Buffers are named HNK and CNK to indicate a combination of HEPES or cacodylate, respectively, together with monovalent sodium and potassium salts. Each buffer was prepared at 22 °C with pH 7.4. All experiments were monitored by RiboGreen fluorescence using DSF. Because HEPES has a temperature-sensitive pKa (-0.014 units/°C), the protonation state of the cytosine involved in the C^+•G-C base triple will change with increasing temperature. The triplex is stabilized as the pH decreases, leading to higher $T_{m,1}$ and $T_{m,2}$ for experiments in HNK buffer relative to those determined in the temperature insensitive cacodylate buffer (see also **Supplementary Figure S1**). Of important note, the difference in T_m is smaller in 0.1 mM $MgCl_2$ relative to 1 mM $MgCl_2$; the RNA is less sensitive to the protonation state of the cytosine under these conditions. This suggests that the triplex is either more dynamic or less folded in 0.1 mM $MgCl_2$, consistent with its degradation by RNase R under this condition (see also **Supplementary Figure S6**).

[$MgCl_2$] (mM)	$T_{m,1}$ (°C)		$\Delta T_{m,1}$ (°C)	$T_{m,2}$ (°C)		$\Delta T_{m,2}$ (°C)
	pH 6.7	pH 7.4	pH 6.7 - pH 7.4	pH 6.7	pH 7.4	pH 6.7 - pH 7.4
0.1	53.7 ± 1.4	51.3 ± 0.4	2.4	72.2 ± 2.1	70.1 ± 0.3	2.05
1.0	64.6 ± 0.1	61.2 ± 0.3	3.4	77.7 ± 0.1	77.1 ± 0.2	0.65

Supplementary Table S2. Stability of M1TH in cacodylate buffer at two pH using UV melt.
Thermal melt experiments at two different concentrations of $MgCl_2$ were performed in the presence of 50 mM monovalent salt (equimolar NaCl and KCl) in 20 mM sodium cacodylate, pH 6.7 at 22 °C or pH 7.4 at 22 °C, and monitored by UV melt. The $T_{m,1}$ and $T_{m,2}$ determined under the different $MgCl_2$ concentrations in pH 6.7 are higher than the corresponding T_m values determined in cacodylate pH 7.4 buffer due to increased protonation of the cytosine in the C^+•G-C triple. Furthermore, the T_m values in cacodylate pH 6.7 buffer are relatively similar to the values determined in HNK buffer pH 7.4 at 22 °C (**Supplementary Table S1**). Small differences in T_m values between this table and those presented in **Supplementary Table S1** are likely due to differences in the experimental ramp rate and signal recorded (DSF vs UV). Overall, the small $\Delta T_{m,1}$ is consistent with the slight lowering of the pH and associated increase in protonation of the cytosine in the C^+•G-C triple. Regardless, the magnitude of change in T_m due to pH is small relative to the overall T_m changes observed in each thermal landscape (DS-FRET, DSF, and UV; see **Table 2** in the main text and **Supplementary Table S4**).

[$MgCl_2$] (mM)	$T_{m,1}$ (°C)		$T_{m,2}$ (°C)	
	UV melt	**DSF**	**UV melt**	**DSF**
0.2	55.6 ± 0.1	56.2 ± 0.2	73.4 ± 0.1	72.1 ± 0.6
1	66.8 ± 0.1	65.7 ± 1.1	78.3 ± 0.1	77.7 ± 0.8

Supplementary Table S3. Comparison of T_m for M1TH from DSF and UV thermal melts.
Thermal melt experiments at two different concentrations of $MgCl_2$ were performed in the presence of 52 mM monovalent salt (equimolar NaCl and KCl) in 20 mM HEPES, pH 7.4 (22 °C), and monitored by UV or RiboGreen fluorescence (DSF). The $T_{m,1}$ and $T_{m,2}$ determined by each method were nearly identical an either $MgCl_2$ concentration. The differences in melting temperature between the two methods is always less than 1.3 °C and are likely due to differences in the temperature ramp rate on the two instruments or small differences in monovalent concentration.

	$T_{m,1}$ (°C)		
	M1^{ET}	**M1^{AB}**	**M1TH**
Maximum signal	60.9	59.5	77.5
Minimum signal	43.3	45.1	55.6
Signal in near- physiological ionic conditions	51.7	53.2	63.3
Relative stability[a]	48%	57%	35%

Supplementary Table S4. Relative triplex stability using UV melt assay.
[a]Relative stability was calculated using [(*P* - *Min*) / (*Max* - *Min*)]*100; where *Max*, *Min*, and *P* indicate maximum signal, minimum signal, and the signal in near-physiologic ionic conditions (1 mM $MgCl_2$ and 202.6 mM total monovalent salt), respectively.

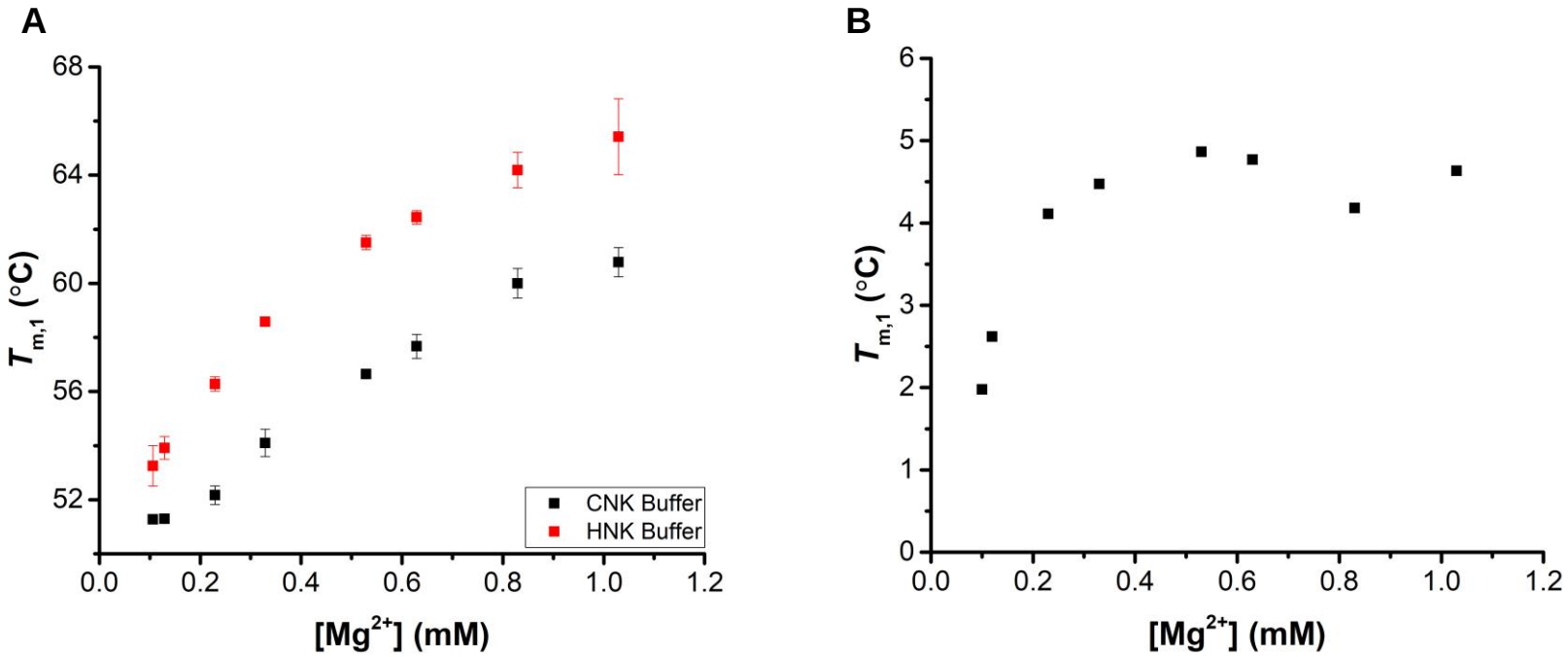

Supplementary Figure S1. A comparison between the thermal stability of M1TH in sodium cacodylate vs. HEPES buffers. (A) DSF melting temperatures of M1TH under different magnesium concentrations (0.11, 0.13, 0.23, 0.33, 0.53, 0.63, 0.83, 1.03 mM) in 50 mM monovalent concentration (equimolar of KCl and NaCl) in two different buffers: 20 mM sodium cacodylate (CNK, black) or 20 mM HEPES (HNK, red), both prepared at pH 7.4 at 23 °C. Error bars represent three independent experiments. The different $T_{m,1}$ values between CNK and HNK buffers are due to the temperature dependence of HEPES pK_a (-0.014 pKa units per °C), which will increase the degree of protonation of the cytosine involved in the C$^+$•G-C triple interaction. Therefore, at higher temperatures this triple will be more stable in HEPES than cacodylate. **(B)** A difference plot of the tertiary melting temperature of M1TH in HEPES buffer compared to sodium cacodylate buffer. Thermal melt experiments performed in HEPES yield higher $T_{m,1}$ values by approximately 2 – 5 °C. From 0.23 mM – 1 mM $MgCl_2$ the difference is consistently ~4.3 °C. The effect is much smaller in 0.11 mM and 0.13 mM $MgCl_2$. Under these low $MgCl_2$ conditions, triplex stability is significantly less responsive to the protonation of the cytosine indicating that the C$^+$•G-C triple is not well formed.

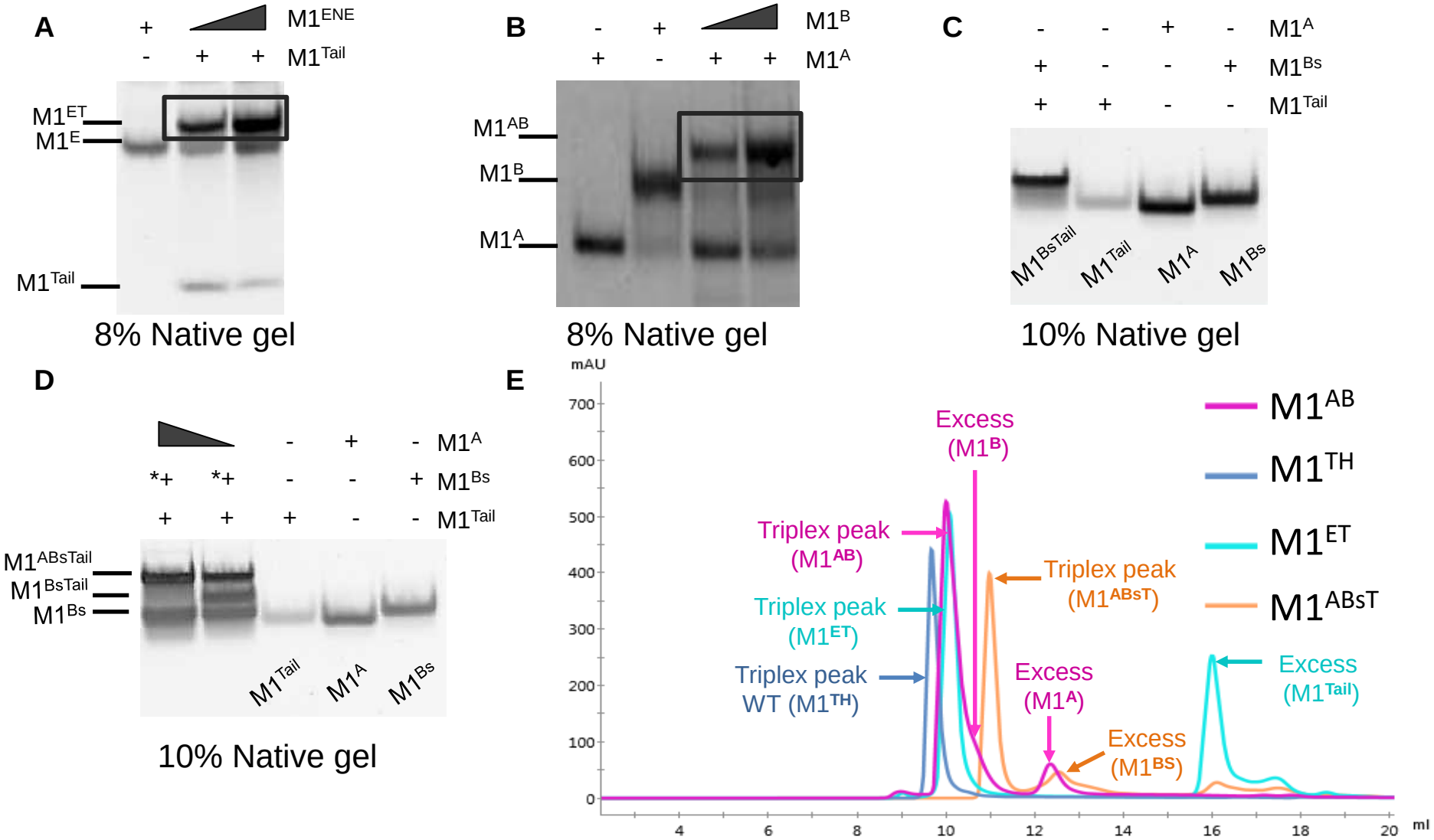

Supplementary Figure S2. The formation of the triple helix with $M1^{TH}$, $M1^{ET}$, $M1^{AB}$, and $M1^{ABsT}$ constructs. Electrophoretic mobility shift assay (EMSA) experiments demonstrating the association of truncated RNA constructs and formation of the triple helix after mixing (**A**) $M1^{ENE}$ with $M1^{Tail}$ (8% native gel), (**B**) $M1^{A}$ with $M1^{B}$ (8% native gel), (**C**) $M1^{Bs}$ with $M1^{Tail}$ (10% native gel) (duplex formation only), and (**D**) $M1^{A}$ with $M1^{Bs}$ and $M1^{Tail}$ (10% native gel), respectively. *+ represents a ration of $M1^{Bs}$ to $M1^{Tail}$ of 2:1. All experiments were conducted in a buffer containing 16.5 mM Tris, 33mM HEPES, 50 µM EDTA and 1 mM $MgCl_2$. **E)** Overlay of the size exclusion chromatograms (SEC) of $M1^{AB}$ (pink), $M1^{TH}$ (blue), $M1^{ET}$ (cyan), $M1^{ABsT}$ (orange) that demonstrates the triple helix formation. Bimolecular constructs $M1^{ET}$ and $M1^{AB}$ have truncated structures and therefore elute after the full-length $M1^{TH}$. $M1^{ABsT}$ is further truncated and elutes after $M1^{ET}$ and $M1^{AB}$. Peaks after 12 ml represent excess short RNA strands (see Methods). SEC purifications were conducted in buffer containing 1 mM $MgCl_2$ and 20mM HEPES, pH7.4.

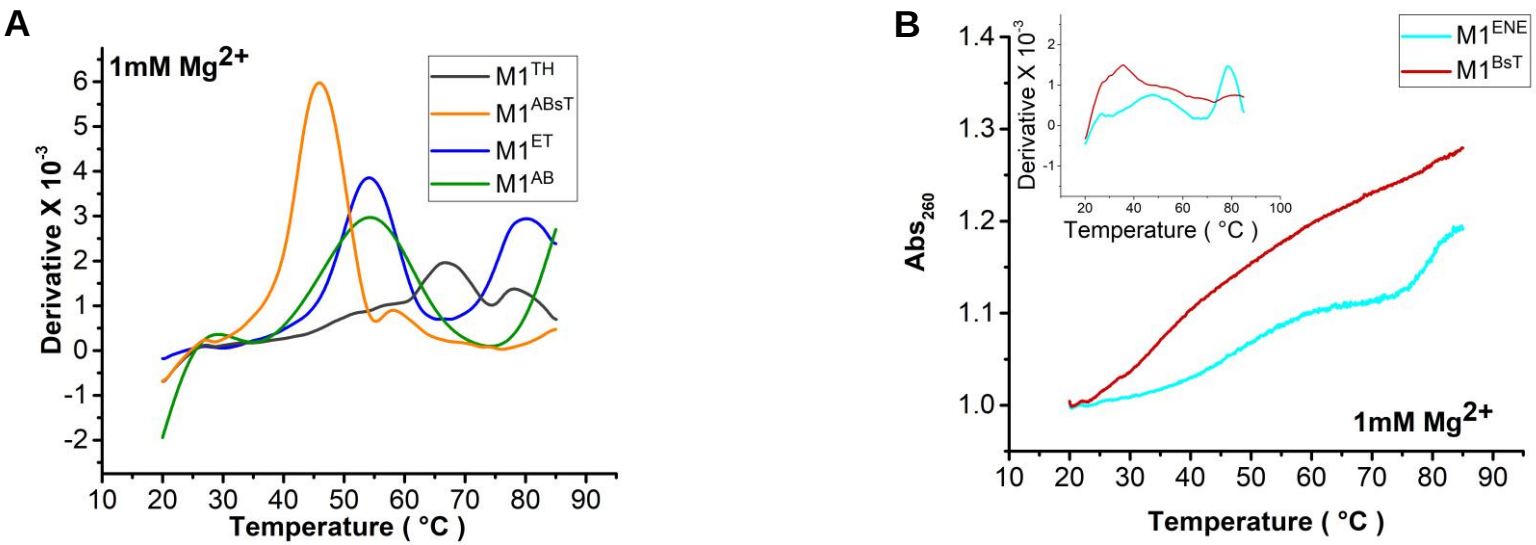

Supplementary Figure S3. Contributions of structural elements on the MALAT1 triple helix thermal stability. (A) Overlay of the first derivative of the raw absorbance signal of $M1^{TH}$, $M1^{ET}$, $M1^{AB}$, and $M1^{ABsT}$ in gray, blue, dark green, and orange, respectively. **(B)** Overlay of the UV melt profiles $M1^{ENE}$ (cyan) and $M1^{BsT}$ (red). **Inset:** Overlay of the first derivative of the raw absorbance signals. An early transition in the ENE (also $M1^{ENE}$) melting profile (~47 °C) suggests residual structure in the U-rich regions and P1 helix in the absence of the A-rich tail. Experiments in (**A**) and (**B**) were conducted in 1 mM $MgCl_2$, 25 mM NaCl, 25 mM KCl in 20 mM HEPES pH 7.4. **(C)** Overlay of the first derivative of $M1^{ET}$ and $M1^{AB}$ at < 0.2mM $MgCl_2$, 25 mM NaCl, 25 mM KCl in 20 mM HEPES pH 7.4 demonstrates a greater loss in triplex stability upon removal of the basal loop ($M1^{ET}$) compared with removal of the apical stem ($M1^{AB}$).

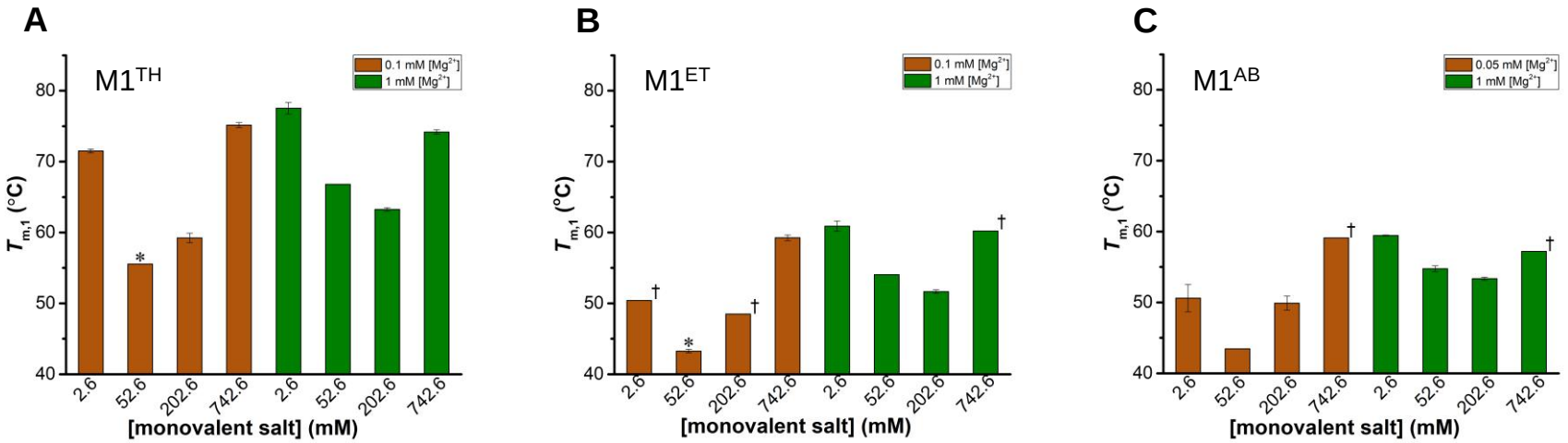

Supplementary Figure S4. Effect of varying monovalent and divalent cations on MALAT1 triple helix stability. **A-C)** Triplex thermal stability ($T_{m,1}$) bar graph generated from triplex melting temperatures monitored by UV thermal melt under different ionic conditions for unimolecular $M1^{TH}$ and bimolecular $M1^{ET}$ and $M1^{AB}$ constructs, respectively. Ionic conditions include 2.6, 52.6, 202.6, and 742.6 mM total monovalent salt (equimolar NaCl and KCl) and 0.05, 0.1, 0.2 and 1 mM $MgCl_2$. Comparison of the tertiary stability for the full-length $M1^{TH}$ with those of the truncated $M1^{ET}$ and $M1^{AB}$ constructs reveals the important role of the peripheral structural elements (linker and P2 helix) in stabilizing the triplex region. At low $MgCl_2$ concentrations, removal of the linker in $M1^{ET}$ is more destabilizing than truncation of the P2 helix in $M1^{AB}$. All experiments were performed in duplicate except those indicated with †, which were performed only once. Brown columns represent experiments at low $MgCl_2$ (0.05, 0.1 or 0.2) mM while green columns represents experiments with 1 mM MgC_2 with ∗ representing experiments performed with 0.2 mM $MgCl_2$, which would result in slightly higher melting temperature compared with the experiments in 0.1 mM $MgCl_2$.

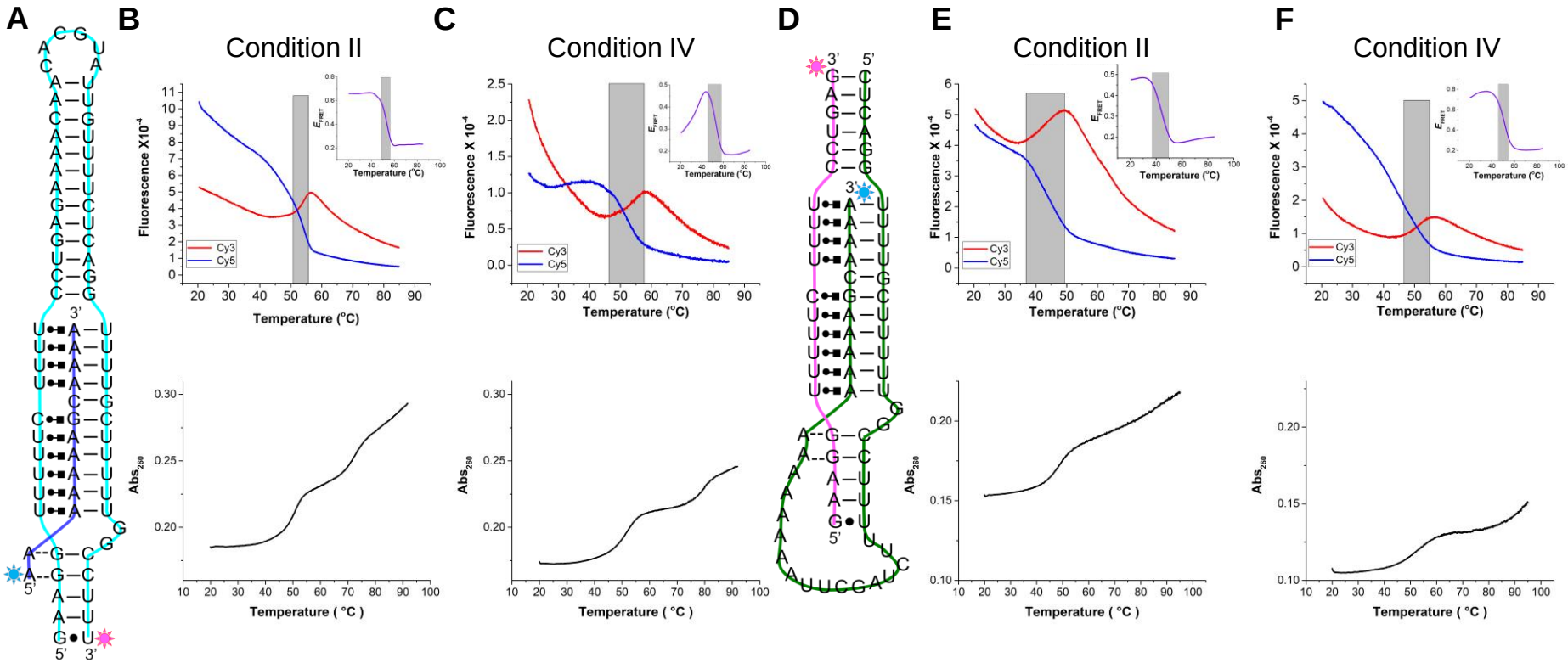

G

M1^{ET}		
	$T_{m,1}$ (°C)	
	Condition II	**Condition IV**
UV melt	50.4	51.3
DS-FRET	53.6	53.3

H

M1^{AB}		
	$T_{m,1}$ (°C)	
	Condition II	**Condition IV**
UV melt	48.4	53.2
DS-FRET	44.3	51.1

Supplementary Figure S5. DS-FRET and UV melt assays reveal different conformations between Condition II and Condition IV. (A) Illustration of dye positions on the secondary structure of $M1^{ET}$ in which the $M1^{ENE}$ motif is shown in cyan and $M1^{Tail}$ is highlighted in blue. Pink and blue stars represent Cy3 and Cy5 dye positions, respectively. **(B)** Thermal melting profiles of $M1^{ET}$ monitored by DS-FRET (top) and UV melt (bottom) at Condition II (2.6 mM, equimolar NaCl and KCl; and < 0.1 mM $MgCl_2$). **(C)** Thermal melting profiles of $M1^{ET}$ by DS-FRET (top) and UV melt (bottom) at Condition IV (~150 mM monovalent salt, equimolar NaCl and KCl; and ~1 mM $MgCl_2$). The increase in E_{FRET} is reproducible over 5 experiments. The fluorophores on this construct are located at the bottom of P1 and bottom of the M1Tail. Over the temperature range up to 45 °C the increase in E_{FRET} is likely due to an initial (partial) unfolding of P1 and the lower portion of the triplex or the A-minor interactions in a manner that brings the fluorophores closer together. At higher temperatures the melting is more complete and the distance between the fluorophores increases, leading to a decrease in E_{FRET}. Comparison of DS-FRET plots in **(B)** and **(C)** demonstrate similar $T_{m,1}$ but distinct raw signals of Cy3 and Cy5, suggesting that the global structural arrangement is not identical. Region of large changes in E_{FRET} are shaded grey. Comparison of the raw UV melt profiles in **(B)** and **(C)** support a distinct relative amount of stacked nucleotides in these two conditions. All UV melt experiments have the same amount of RNA (6.7 µg/mL). **(D)** Secondary structure of $M1^{AB}$ in which $M1^{A}$ is shown in pink and $M1^{B}$ is shown in green. Pink and blue stars represent donor and acceptor dyes positions in which donor and acceptor dyes are Cy3 and Cy5, respectively. **(E)** Thermal melting profiles of $M1^{AB}$ by DS-FRET (top) and UV melt (bottom) at Condition II (2.6 mM , equimolar NaCl and KCl; and < 0.1 mM $MgCl_2$). **(F)** Thermal melting profiles of $M1^{AB}$ by DS-FRET (top) and UV melt (bottom) at Condition IV (~150 mM monovalent salt, equimolar NaCl and KCl; and ~1 mM $MgCl_2$). Region of large changes in E_{FRET} are shaded grey. Comparison between the two conditions of raw DS-FRET or UV melt signals demonstrates distinct fluorescence or relative absorbance signals, respectively, across the melting profile in these two conditions. All UV melt have the same amount of RNA (5 µg/mL). (**G**) and (**H**) Summary of the $T_{m,1}$ values from DS-FRET and UV melts in Conditions II and IV.

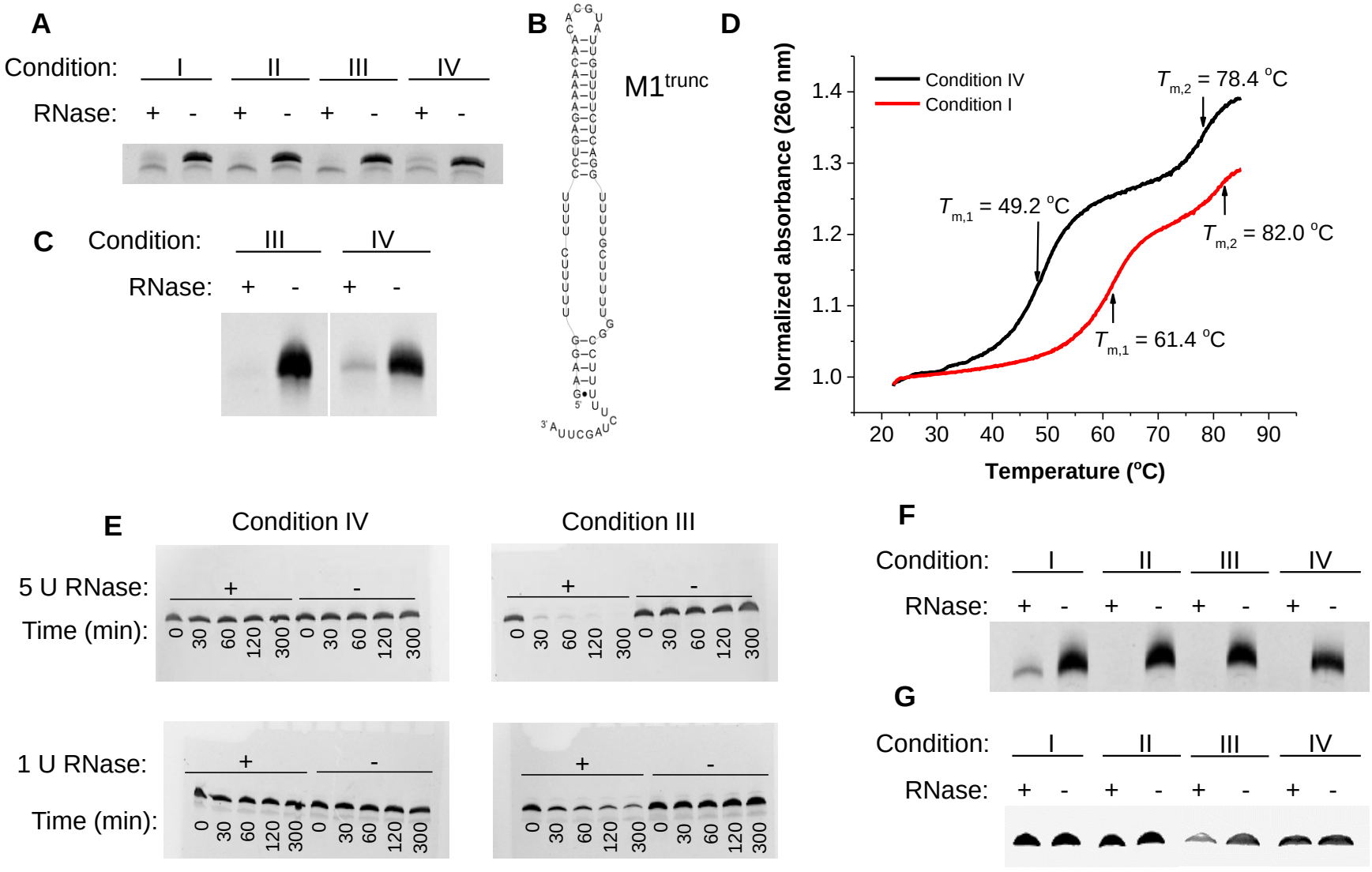
A
Condition: I II III IV
RNase: + - + - + - + -
B
M1trunc
C
Condition: III IV
RNase: + - + -
D
Condition IV
Condition I
$T_{m,2}$ = 78.4 °C
$T_{m,1}$ = 49.2 °C
$T_{m,2}$ = 82.0 °C
$T_{m,1}$ = 61.4 °C
Normalized absorbance (260 nm)
1.0
1.1
1.2
1.3
1.4
20 30 40 50 60 70 80 90
Temperature (°C)
E
Condition IV
Condition III
5 U RNase:
1 U RNase:
Time (min):
+ -
0 30 60 120 300 0 30 60 120 300
F
Condition: I II III IV
RNase: + - + - + - + -
G
Condition: I II III IV
RNase: + - + - + - + -

Supplementary Figure S6. Mutated and disrupted triplexes are susceptible to degradation by RNase R. (A) An unstructured 94-nt ssRNA is completely degraded by RNase R under all conditions tested. The lower band that is present in all lanes and resists degradation by RNase R is DNA, which is degraded by DNase (data not shown). Condition I contains 2.6 mM KCl and 1 mM Mg^{2+}, Condition II contains 2.6 mM KCl and 0.1 mM Mg^{2+}, Condition III contains 52.6 mM total monovalent salt (equimolar NaCl and KCl) and 0.1 mM Mg^{2+}, and Condition IV contains 152.6 mM total monovalent salt (equimolar NaCl and KCl) and 1 mM Mg^{2+}. **(B)** A schematic diagram of the secondary structure of $M1^{trunc}$ in which the A-rich tail is removed. **(C)** $M1^{trunc}$ is efficiently degraded by RNase R under all conditions tested (Conditions III and IV). **(D)** Thermal melting profiles of $M1^{polyA}$ under Condition IV (black trace) and Condition I (red trace) show that the mutant is thermodynamically stable, despite its susceptibility to degradation by RNase R. **(E)** Degradation time-course of $M1^{TH}$ in the presence of either 5 U (top panels) or 1 U (bottom panels) RNase R per 0.5 µg RNA. Under Condition IV, $M1^{TH}$ is completely protected from degradation, even in the presence of high concentrations of enzyme. Under Condition III, $M1^{TH}$ is incompletely degraded by low concentrations RNase R over 5 hours, but is completely degraded within 30 minutes by high concentrations of RNase R. **(F)** $M1^{polyA}$ is degraded under all conditions tested by 1 U of RNase R. **(G)** $M1^{TH}$ is degraded by 1 U of RNase R under Condition III, but is protected from degradation under Conditions I, II, and IV).

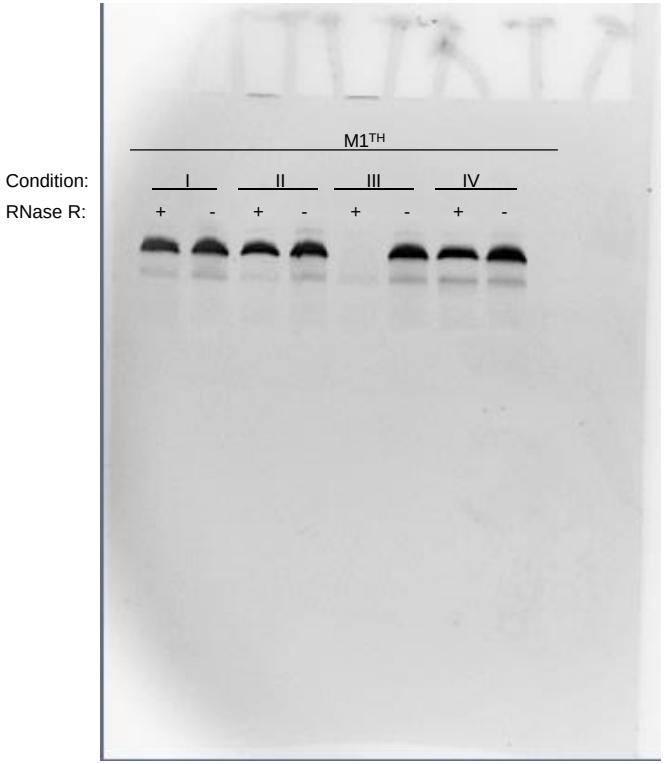

Supplementary Figure S7. RNase R completely degrades M1TH under Condition III. The full-size gel image of M1TH treatment with RNase R shown in Figure 4D demonstrates that under Condition III (0.1 mM $MgCl_2$, 52.6 mM monovalent salt) M1TH is completely degraded to mononucleotides. Following 5-hour incubation of RNA with RNase R, reactions were run on a 6% denaturing PAGE at 30 W for 50 minutes, followed by staining with ethidium bromide. The gel was run under conditions in which a 25-nt oligomer would be about half-way down the gel. Mononucleotides would be located at the bottom of the gel but are not visible by ethidium bromide staining. Intermediate length oligomers resulting from incomplete degradation by the exoribonuclease are not observed, either because they are too short to be stained by ethidium bromide or because there are none present. The band just below the 94-nt full-length M1TH is a DNA template, as in **Supplementary Figure 6A**. It is present in all samples and is not a degradation product.

References

1. Brown, J.A., Valenstein, M.L., Yario, T.A., Tycowski, K.T. and Steitz, J.A. (2012) Formation of triple-helical structures by the 3'-end sequences of MALAT1 and MENβ noncoding RNAs. *Proc. Natl. Acad. Sci. U.S.A.*, **109**, 19202-19207.
2. Mitton-Fry, R.M., DeGregorio, S.J., Wang, J., Steitz, T.A. and Steitz, J.A. (2010) Poly(A) tail recognition by a viral RNA element through assembly of a triple helix. *Science,* **330**, 1244-1247.
3. Brown, J.A., Bulkley, D., Wang, J., Valenstein, M.L., Yario, T.A., Steitz, T.A. and Steitz, J.A. (2014) Structural insights into the stabilization of MALAT1 noncoding RNA by a bipartite triple helix. *Nat. Struct. Mol. Biol.*, **21**, 633-640.
4. Brown, J.A., Kinzig, C.G., DeGregorio, S.J. and Steitz, J.A. (2016) Hoogsteen-position pyrimidines promote the stability and function of the MALAT1 RNA triple helix. *RNA*, **22**, 743-749.
5. Brown, J.A., Kinzig, C.G., DeGregorio, S.J. and Steitz, J.A. (2016) Methyltransferase-like protein 16 binds the 3′-terminal triple helix of MALAT1 long noncoding RNA. *Proc. Natl. Acad. Sci. U.S.A.*, **113**, 14013-14018.
6. Letai, A.G., Palladino, M.A., Fromm, E., Rizzo, V. and Fresco, J.R. (1998) Specificity in formation of triple-stranded nucleic acid helical complexes: Studies with agarose-linked polyribonucleotide affinity columns. *Biochemistry*, **27**, 9108-9112.